AIAA 2004-2244

34th AIAA Fluid Dynamics Conference and Exhibit
28 June - 1 July 2004, Portland, Oregon

AIAA Paper 2004-2244

Numerical Simulation and Experimental Comparison of Hypersonic Boundary Layer Instability over a Blunt Cone

Xiaolin Zhong *
University of California, Los Angeles, California 90095

The linear stability of Mach 7.99 flow over a 7° half-angle blunt cone, which corresponds to Stetson et al.'s (AIAA paper 84-0006) boundary-layer stability experiments, is studied in this paper by comparing the results of numerical simulation, experiments, and linear stability analysis (LST). The receptivity to wall blowing/suction at three different surface locations is used to excite the second mode instability waves in the numerical simulation of the full Navier-Stokes equations. The purpose of this study is to evaluate the long-standing disagreement on the second-mode growth rates between Stetson's experimental results and those predicted by the linear stability theory (LST). The validation of the accuracy of LST and numerical simulation is of practical significance because LST calculations are the foundation of the e^n transition prediction method. In addition, the code validation studies are important because numerical simulation has become a powerful tool in studying high speed boundary layer stability and transition It is found that the second-mode growth rates and wave numbers of LST agree well with those computed by numerical simulation. The experimental second-mode amplitude growth ratios, N factors, and growth rates agree reasonably well with those of the simulation in the "linear growth region" of $195 \leq s \leq 215$ for frequencies near the peak second mode instability. It is concluded that the simulation and LST are accurate in predicting second mode growth in the current hypersonic boundary layer flows. The receptivity simulation results also show that strong excitation of the second mode can occur only when the blowing/suction slot is located upstream of the synchronization location between the stable mode I and the second mode.

I. INTRODUCTION

The prediction of laminar-turbulent transition in hypersonic boundary layers is a critical part of the aerodynamic heating analyses on hypersonic vehicles. Despite decades of extensive research, the prediction of hypersonic boundary-layer transition is still based on mostly empirical correlation methods or the semi-empirical e^n method. Most of our current knowledge on hypersonic boundary-layer stability and transition is based on the results of linear stability theory (LST),[1] which concerns with the linear growth or decay of boundary-layer normal modes. Mack[1] showed that the stability characteristics of high supersonic and hypersonic boundary layers are very different from those of subsonic boundary layers. He found that, in addition to the first-mode instability waves, there are higher acoustic instability modes in hypersonic boundary layers. Among the instability wave modes in hypersonic boundary layers, the second mode becomes

*Professor, Mechanical and Aerospace Engineering Department, Associate Fellow AIAA. E-mail: xiaolin@ucla.edu.

the dominant instability at hypersonic Mach numbers. The second mode instability is particularly important for practical hypersonic flight applications where the free-stream disturbances are often very weak. Under such conditions, the by-pass transition is not likely, and the second mode instability is a dominating instability before the transition of the boundary layers. The existence and dominance of the second mode instability in hypersonic boundary layers has been observed in boundary-layer stability experiments for hypersonic flows over sharp or blunt cones.[2–6]

The LST analysis is the foundation of the e^n method for boundary-layer transition prediction, which assumes that the transition is a result of linear exponential growth of the most unstable normal mode. For supersonic and hypersonic boundary layers, the most unstable mode is the first Mack mode at relatively low Mach numbers and the second Mack mode at Mach numbers higher than about 4. The transition criteria used in the e^n method are established based on the evaluation of a N factor which is defined as, $\log(\frac{A}{A_{ref}})$, where A/A_{ref} is the ratio of the wave amplitudes of the most unstable mode. The value of N can be computed by LST. Transition is assumed to take place when N is larger than a certain empirical value. The e^n transition prediction based on the normal-mode instability analyses works well for flow in a relatively quiet environment, where transition is not caused by transient growth or other by-pass transition mechanisms. The success of the e^n method depends on, among other factors, the conditions that the transition is caused by the linear growth of the most unstable mode and the growth rates of the most unstable mode can be accurately predicted by LST. In addition, the e^n method also has a drawback that the initial generation of the unstable modes, which is the subject of a receptivity study, is not considered. Because the wave growth and transition in boundary layers depend on the initial amplitudes of the wave modes, e^n transition prediction methods without the consideration of the forcing disturbances and the subsequent wave mode generation by the receptivity processes are not satisfactory.

The experimental validation of the LST and the numerical simulation based on the full Navier-Stokes equations results on the second mode instability for hypersonic boundary layers are the subject of this papers. For hypersonic boundary layers, there are not many available stability experiments which can be used for the validation purpose. NATO RTO Working Group 10 on Boundary Layer Transition[7] identified three best available stability experiments for CFD code validation on hypersonic boundary layer transition. One of these cases that has been extensively studied by LST is the Mach 7.99 blunt cone experiment by Stetson et al.[4,6] Stetson et al. carried out boundary-layer stability experiments on an axisymmetric blunt cone in a Mach 7.99 free stream (Fig. 1). The half angle of the cone was 7°, the nose radius was $3.81 \times 10^{-3}m$, and the free-stream Reynolds number based on the nose radius was 33,449. The total length of the cone was about 270 nose radii, corresponding to a Reynolds number of about 9 millions. Detailed fluctuation spectra of the disturbance waves developing along the body surface were measured in the experiments. It was found that the disturbances in the boundary layer were dominated by the second mode instability. Significant super harmonic components of the second modes were observed after the second mode became dominant. Compared with similar hypersonic flow over a sharp cone, the second mode instability of the blunt cone appeared in much further downstream locations. This indicates a stabilization of the boundary layer by slight nose bluntness. Stetson et al. also found evidence of entropy-layer instability in the region outside the boundary layer in a test case of larger nose radius.

In addition to Stetson's work, only a few stability experiments of hypersonic flows over sharp or blunt cones have been carried out by other researchers. Kendall measured boundary layer stability for supersonic and hypersonic flow over a flat plate for Mach numbers between 1.6 and 8.5.[8] Demetriades[2,3] did extensive stability experiments on hypersonic boundary layers over axisymmetric cones. Chokani and his colleagues did stability measurements on Mach 6 flow over a flared cone in a quiet tunnel.[9–11] Recently, Maslov and his colleagues[5] conducted their stability experiments on Mach 5.92 flow over sharp and blunt cones. Maslov et al. measured the fluctuation spectra of the disturbance waves in the boundary layer.

The normal-mode linear stability characteristics of the boundary-layer flow over the blunt cone of Stetson et al.'s experiments have been studied by a number of researchers.[12–20] Malik et al.[12] computed the neutral stability curve and compared the growth rates obtained by LST with the experimental results. The steady base flow solution was computed by using the parabolized Navier-Stokes equations. They found that the

nose bluntness stabilizes the boundary layer second mode. The growth rates of the first and second modes predicted by the LST were compared with Stetson et al.'s experimental results at the surface location of $s = 175$ and $s = 215$ nose radii. The linear stability analyses predicted slightly lower frequency for the dominant second mode, but about 60% higher in the peak amplification rate than the experimental results. Esfahanian and Herbert[13] conducted similar base flow and LST calculations for the same flow by using a much finer grid resolution. Their LST results at the same $s = 175$ surface station agree reasonably well with those of Malik et al. In a separate study, Kufner et al.[14,15] did extensive LST calculations for the same flow over the blunt cone. Further LST calculations for the same flow have also been carried out, using various numerical methods, by Rosenboom et al.,[16] Zhong and Ma,[18,19] and Lyttle et al.[20] Figure 2 was obtained by Zhong and Ma[18,19] compares the second mode growth rates predicted by the LST and by experiments of Stetson et al. The figure shows that there are only small variations in the LST growth rates obtained independently by these different group of authors. The small variations among these different sets of LST growth rates are possibly caused by differences in their mean flow solutions and slight differences in their freestream flow conditions. However, all LST results consistently predicted much higher growth rates than those of the stability experiments at the 175 nose radii surface station. It was speculated that the discrepancy is a result of the nonlinear effects in the experimental wave fields because there are significant super harmonic components in the experimental results. On the other hand, the nonlinear effects are neglected in the linear stability analysis.

For the purpose of CFD code validation, Schneider[17,21] published additional stability experimental results of Stetson's 1984 experiment for the same blunt cone. He compared the amplification ratios, instead of growth rates, of the new published Stetson's experimental data with the LST results computed by Kufner. The region of the comparison was chosen to be between surface stations of 215 and 195 nose radii. He argued that this region is best for comparison with linear stability results because the second harmonics in the experimental results are not very significant while the instability modes are clearly above the background noise in the experimental results. He found much better agreement between the LST and the experimental results (within 10% percent). It is believed that the poor agreement in the $s = 175$ surface station is caused by fact that the instability wave signal is contaminated by the relatively high background noise.

Lyttle et al.[20] did further LST calculations to compare with the Stetson's experimental results on the linear-growth region ($195 \leq s \leq 215$) in the experimental results. Since the experiments did not have perfect adiabatic wall, they also investigated the effects of wall cooling on the LST comparisons. Figure 10 of Lyttle et. al.[20] shows that the peak N factor between 215 and 195 surface stations predicted by their LST agree reasonably well with those of the Stetson's experiments. The amplification rates were not compared in the "linear-growth region". They concluded that the traditional experimental-LST disagreement in growth rates at $s = 175$ may be due to insufficient amplification of the experimentally-measured disturbances. These comparisons are promising in showing the validity of the LST calculations. But the comparisons are limited because of the limited experimental results available. Numerical simulation of the Navier-Stokes equations for hypersonic boundary instability, on the other hand, can fill the gap between LST and experimental results because complex physical effects and interactions neglected by theoretical analyses are taken into account in a numerical simulation of the full Navier-Stokes equations. In addition, numerical simulation can provide large amount of additional flow information which are useful not only for understanding new hypersonic boundary stability mechanisms, but also for evaluating the accuracy of LST results for hypersonic boundary-layer stability.

Therefore, the objective of this paper is to conduct a numerical simulation study of the second mode instability of the Mach 7.99 flow over Stetson's blunt cone. The simulation results are compared with both LST and experimental results. The focus is on the second mode growth and comparison. In the numerical simulation, the second mode waves are induced by imposing a blowing/suction in a narrow surface section. The growth rates, wave numbers, wave speeds,and N factors are compared with the LST and experimental results. The LST calculations in this paper are carried out by using a new axisymmetric LST code developed by Zhong and Ma[18,19] to study the linear stability properties of the axisymmetric boundary layer.

The current study follows previous studies by the author on the freestream receptivity of the same

hypersonic flow over the blunt cone.[18,19] Zhong and Ma[18,19] conducted a numerical study on the receptivity to free-stream acoustic waves for same Stetson's hypersonic flow with the effects of nose bluntness and the entropy layer. In the numerical simulation, both steady and unsteady flow fields between the bow shock and the boundary layer are numerically simulated by using a high-order shock-fitting scheme,[22] which has been extensively tested for its accuracy in accounting for the effects of bow-shock/free-stream-disturbance interactions in a transient flow computations. The effects of nose bluntness, entropy layer, shock-disturbance interaction, non-parallel boundary layers and surface curvature on the receptivity process are accurately taken into account by the high-order shock-fitting scheme. It was found that the steady flow solution of the full Navier-Stokes equations agrees very well with those computed by Esfahanian and Herbert[13] by using the thin-layer Navier-Stokes equations. In addition, the solution of Zhong and Ma agrees well with Stetson et al.'s experimental results on surface pressures, bow shock locations, and tangential velocities outside the boundary layer. Having obtained the steady base flow solution, the receptivity to free-stream fast acoustic waves was investigated by numerical simulation. A total of 15 frequencies have been considered in the freestream receptivity simulation. It was found that, similar to the flat plate boundary layer cases[23,24], the basic receptivity mechanisms of the current axisymmetric hypersonic flow over a blunt cone are resonant interactions between the forcing waves and boundary-layer wave modes, and resonant interactions among different boundary-layer wave modes. The validation study of this paper extends the previous receptivity studies by investigating the second mode receptivity to wall blowing/suction by numerical simulations, and by simulation-experiment-LST comparisons on the second mode growth.

II. EQUATIONS, NUMERICAL METHODS & FLOW CONDITIONS

Steady and unsteady axisymmetric hypersonic flow over a blunt cone are simulated by a fifth-order shock-fitting scheme in computing the full Navier-Stokes equations. Since the same governing equations, physical models, and numerical method used are the same as those of Zhong and Ma[18,19], the details of the governing equations and numerical methods are not presented here.

In this paper, the flow variables are nondimensionalized using the free-stream conditions as characteristic variables. Specifically, we nondimensionalize the flow velocities by the free-stream velocity U_∞^*, length scales by L^* which is either the nose radius r_n^* or boundary layer thickness scale described later in the paper, density by ρ_∞^*, pressure by p_∞^*, temperature by T_∞^*, time by L^*/U_∞^*, wave number by $1/L^*$, etc. The dimensionless flow variables are denoted by the same dimensional notation but without the superscript "$*$".

The flow conditions for the test case studied in this paper are the same as those of Stetson et al.'s experiments on air flow over a blunt cone. The specific flow conditions are:

$M_\infty = 7.99$, $Re_{r_n} = \rho_\infty^* U_\infty^* r_n^* / \mu_\infty^* = 33,449$
$p_t^* = 4 \times 10^6\ Pa$, $T_t^* = 750\ K$
$\gamma = 1.4$, $Pr = 0.72$, $R^* = 286.94\ Nm/kgK$
Free-stream unit Reynolds number: $Re_\infty^* = 8.78 \times 10^6\ m^{-1}$
Blunt cone half angle: $\theta = 7^\circ$, zero flow angle of attack.
Spherical nose radius: $r_n^* = 3.81 \times 10^{-3}\ m$
Parameters in Sutherland's viscosity law: $T_r^* = 288\ K$, $T_s^* = 110.33\ K$,
$\mu_r^* = 0.17894 \times 10^{-4}\ kg/ms$.

The body surface is a no-slip and adiabatic wall for the steady base flow solution. The total length of the cone of the experimental model is $l^* = 1.016\ m$ (267 nose radii). The simulation covers the entire flow field from the nose to about 330 nose radii downstream. The origin of the Cartesian coordinate system, (x, y, z), is located at the center of the nose spherical cone, where the x coordinate points from left to the right in Fig. 1 along the the center line of the axisymmetric cone. In addition to x, a natural coordinate s is also used in the experiment to measure the dimensionless curve length of a surface location started from the stagnation point. The non-dimensional s and x, which are normalized by the nose radius r_n^*, are related to each other

by the following relation:

$$x = \begin{cases} -\cos(s) & (s \le \frac{\pi}{2} - \theta) \\ (s - \frac{\pi}{2} + \theta)\cos\theta - \sin\theta & (s > \frac{\pi}{2} - \theta) \end{cases} \quad (1)$$

In the experiments of Stetson et al., the wall surface was close to, but not exactly, adiabatic. The actual surface temperatures were about 10% to 20% lower than those of an adiabatic wall in the same free stream. The stability and receptivity properties of hypersonic boundary layers are strongly affected by the changes of surface temperatures. In this paper, only the case of an adiabatic wall for the steady base flow is considered. The case of an adiabatic wall is chosen because most previous LST studies on the same flow were based on the assumption of the adiabatic wall.

III. GENERAL LINEAR STABILITY PROPERTIES

The numerical simulations results are compared with LST results on second mode growth rates and wave numbers. An axisymmetric LST computer code of Zhong and Ma[19] is used for analyzing the linear stability properties of axisymmetric compressible boundary layers in this paper. In the LST, a local Reynolds number, R, based on the length scale of boundary-layer thickness is used:

$$R = \frac{\rho^*_\infty u^*_\infty L^*}{\mu^*_\infty} \quad (2)$$

where L^* is the length scale of boundary-layer thickness defined as

$$L^* = \sqrt{\frac{\mu^*_\infty s^*}{\rho^*_\infty u^*_\infty}} \quad (3)$$

where s^* is the natural surface coordinate defined as the curve length along the wall surface measuring from the nose. The nondimensional frequency ω and wave number α are normalized by u^*_∞ and L^* :

$$\alpha = \alpha^* L^* \quad (4)$$

$$\omega = \omega^* L^* / u^*_\infty \quad (5)$$

The forcing frequency is represented by a dimensionless frequency F defined by

$$F = 10^6 \frac{\omega^* \nu^*}{U^{*2}_\infty}. \quad (6)$$

The dimensionless frequency F is related to ω by

$$\omega = 10^{-6} F R \quad (7)$$

For a given value of F and surface location s, ω can be computed by the equation above. The real part of wave number α_r is related to phase velocity of a wave mode by

$$a = \frac{\omega}{\alpha_r} = \frac{10^{-6} F R}{\alpha_r} \quad (8)$$

where a is the nondimensional phase velocity normalized by the free-stream velocity.

The flow disturbances in the axisymmetric boundary-layer flow are represented by the perturbations of instantaneous flow variables with respect to their local base flow solution. The LST is based on the normal

mode analysis under a local parallel flow assumption. Specifically, the linear fluctuations of flow variables are decomposed into the following normal mode form:

$$q' = \hat{q}(y_n)\, e^{i\,(-\omega t + \alpha\, s)} \tag{9}$$

where $\hat{q}(y_n)$ is the complex amplitudes of the disturbances, y_n and s are the local natural coordinates along the wall-normal and surface directions respectively, $\alpha = \alpha_r + i\alpha_i$, is the streamwise complex wave number, and ω is the circular frequency. The variable q stands for any of the independent flow variables u, v, w, p, ρ (or T). In a spatial linear stability analysis, for a given frequency ω, complex parameter α and complex function $\hat{q}(y)$ are obtained as an eigenvalue and eigenfunction of the stability equations. For a spatial stability problem, ω is a real number while α is a complex wave number. The real and imaginary parts of α, α_r and α_i, represent the spatial wave number and growth rate of a wave mode respectively. A linear wave mode is unstable when α_i is negative.

The general linear stability behavior of the current hypersonic boundary layer are shown in Figs. 2 to 4, which are obtained by our previous study.[19] Figure 2 compares spatial growth rates for the current axisymmetric Mach 7.99 flow at the surface station of $s = 175$. The experimental results of Stetson et al., and several other published LST results (Malik et al.,[12] Herbert & Esfahanian[13]), are plotted in the same figure for comparison. The figure shows that the current LST results on the second-mode growth rates ($100kHz < f^* < 170kHz$) compare well with the other LST results. The differences between the current LST results and those of other authors are mainly caused by different steady base flow solutions used in different LST computations. In this figure, the growth rates of the first mode in the current calculations are for two-dimensional disturbances only, while those of Malik et al. are the most unstable oblique first mode.

The previous LST studies on the axisymmetric hypersonic boundary layer over Stetson's blunt cone mainly focused on the calculations of the growth rates of the unstable first and second Mack modes. Other boundary-layer wave modes, which are always stable, have not been studied. In Ma and Zhong's receptivity study of Mach 4.5 boundary-layer flow over a flat plate[23–25], it was found that a family of other wave modes, which are always stable in a linear stability analysis, play an important role in the receptivity process. They were termed mode I, II, III, etc. Figure 3 shows the distributions of the phase velocities of three discrete modes, mode I, mode II and the Mack modes (including the first and the second modes), as functions of frequencies at a fixed surface station of $s = 175$. The phase velocities of the fast acoustic wave $(1 + 1/M_\infty)$, entropy/vorticity wave (1), and slow acoustic wave $(1 - 1/M_\infty)$ are also shown in the figure for comparison. Both mode I and mode II originate from the fast acoustic wave limit with an initial phase velocity of the fast acoustic wave at $1 + 1/M_\infty$. Before these two modes become distinct it was found[19] that, at the intersection point between mode I and the first mode ($\omega = 0.1825$ for $s = 175$), mode I is synchronized with the Mack mode because the two modes have the same frequency, phase velocity and wave number. Therefore, there is a resonant interaction between mode I and the Mack mode near this resonant interaction location. The unstable region of the second mode is in the range of ω between 0.171 and 0.243 ($116.7kHz < f^* < 165.9kHz$) of the Mack modes shown in the figure. In this range, the growth rates of the second mode increases to a peak and decays afterward. The second Mack mode has the largest growth rate at $\omega = 0.198$ ($f^* = 135kHz$) at the surface station of $s = 175$.

Fedorov and Khokhlov[26] did a theoretical analysis of the receptivity of hypersonic boundary layers to wall disturbances. They found that a strong excitation occurs in local regions where forcing is in resonance with boundary layer normal waves. There is an extremely high receptivity to blowing/suction in the vicinity of the synchronization point, which is marked in Fig. 3. In order to effectively excite the second mode, the blowing/suction location needs to be before or near the synchronization point between mode I and the second mode. The numerical simulation can be used to study the receptivity to wall disturbances in order to validate Fedorov's theory.

The neutral stability curve of the Mack modes computed by the current LST code is compared with that of Malik et al.[12] in Fig. 4. Dimensional frequencies f^* are used in the figure because the experimental results were presented using dimensional frequencies. The synchronization locations between mode I and the Mack

modes are also plotted in the same figure. There are two peaks in the neutral stability curve. The first peak with lower frequencies (lower than 100 kHz) is for the first Mack mode instability, while the second peak with higher frequencies (higher than 100 kHz) is for the second mode instability. Overall, this figure shows a reasonable agreement between the present result and Malik's result in the neutral stability curve.

IV. SIMULATION OF RECEPTIVITY TO WALL BLOWING/SUCTION

In the simulation, the second mode instability waves in the boundary layer are induced by the blowing and suction in a narrow surface strip in the upstream region of the surface. Since the wave fields in the experiment contain a wide range of second-mode frequencies, we introduce, by surface blowing and suction, disturbances of a mixture of number of frequencies near the dominant second mode waves in the simulation. The subsequent receptivity and development of the instability waves at these frequencies are computed by the numerical simulation. The specific formulas for surface blowing and suction in a narrow upstream range are given by the perturbations to the wall normal velocity, i.e.,

$$v_n(x,t) \quad = \quad \epsilon \sin[\alpha_w(x-x_0)] \sum_{n=0}^{N} A_n \cos(n\omega_1 t + \phi_n) \qquad\qquad (x_0 \le x \le x_1) \tag{10}$$

where ϵ is a small nondimensional number representing forcing disturbance amplitudes. The specific forcing waves introduced by blowing and suction are a mixture of $N = 15$ independent frequencies, i.e.,

$$f_n^* \quad = \quad n\ f_1^* \qquad\qquad (n = 1, 2, \cdots, N; N = 15) \tag{11}$$

where the lowest frequency is $f_1^* = 14.92kHz$ ($F_1 = 9.04$). The remaining 14 frequencies are multiples of f_1^* given by Eq. (11), where the highest frequency is $f_{15}^* = 223.8kHz$ ($F_{15} = 135.5$).

The distribution of the relative amplitudes of the free-stream waves among different frequencies is the same as those used in the freestream receptivity study.[18,19] Since the wave components of different frequencies are linearly independent, the initial phase angles, ϕ_n at frequency $\omega_n = n\omega_1$ are chosen randomly. The 15 sets of wave frequencies, relative amplitudes A_n, and phase angles used in the current receptivity simulation are listed in Table 1.

Since the purpose is to study the linear stability of the boundary layer, ϵ is chosen to be small enough so that the boundary response to the forcing disturbances is linear. In the simulation, the overall forcing wave amplitude used in the simulation is

$$\epsilon \quad = \quad 10^{-7} \tag{12}$$

which is small enough that the receptivity process falls in the linear regime. Consequently, the wave components of 15 frequencies are independent, and they can be decomposed one from another by a temporal Fourier analysis. In addition, because the forcing waves are linear, the use of normal velocity perturbations on the surface does not introduce net mass flux into the flow field by the blowing/suction slot.

Although the steady base flow has an adiabatic wall with a zero temperature gradient on the wall, it has been generally accepted that the temperature perturbations should be set to zero because of the relatively high frequencies of the second mode. In the current study, zero temperature perturbation condition, $T' = 0$, is used for both LST and for the unsteady flow simulation of full Navier-Stokes equations.

V. RESULTS

A. Three Cases of Receptivity to Wall Blowing/Suction

In the current study, a number of independent sets of simulations have been carried out for the case of receptivity to wall blowing and suction. Each case uses the same flow conditions and the same forcing

Table 1. Forcing acoustic wave components of 15 frequencies in the surface blowing/suction slot.

n	f_n^* (kHz)	F_n	A_n	$\phi_n(radian)$	s_{syn} (Syn. Pt.)
1	14.92	9.035	0.7692	2.4635(-6)	12196.8
2	29.84	18.07	0.4162	0.1600	3049.2
3	44.77	27.11	0.2827	2.2149	1355.2
4	59.68	36.14	0.2065	4.1903	762.3
5	74.61	45.18	0.1707	6.0510	487.8
6	84.53	54.21	0.1406	5.2671	338.8
7	104.5	63.25	0.1132	2.1070	248.9
8	119.4	72.28	9.7164(-2)	5.7511	190.6
9	134.3	81.31	0.1081	5.0005	150.6
10	149.2	90.35	9.0781(-2)	5.2319	122.0
11	164.1	99.39	7.7722(-2)	2.1679	100.8
12	179.1	108.4	5.8428(-2)	5.4738	84.7
13	194.0	117.5	5.0729(-2)	0.5649	72.2
14	208.9	126.5	7.6987(-2)	5.5812	62.2
15	223.8	135.5	5.7108(-2)	4.4043	54.2

strength and frequencies, except that the location of the blowing/suction strip (x_0 in Eq. (10)) is different. The purpose is to investigate the effects of blowing/suction location on the receptivity of the second mode to wall perturbations. The width of the blowing and suction strip is set to a constant of 2.5 nose radius for all cases. Only the results of three representative cases are presented in this paper. The three cases are:

Case 1: $x_0 = 100$, Exit Location of Simulation: $s = 327$
Case 2: $x_0 = 150$, Exit Location of Simulation: $s = 327$
Case 3: $x_0 = 210$, Exit Location of Simulation: $s = 327$

As shown in Fig. 3, the synchronization point has a nondimensional frequency of $\omega = 0.1825$, a wave speed of $a = 0.916$, and the corresponding wave number of $\alpha_r = 0.19924$. Though Fig. 3 is for the surface station of 175 nose radius only, Ma and Zhong[23,24] showed that the nondimensional phase speed as a function of ω is independent of frequency F and surface locations s. It is expected that Fig. 3 also applies to other surface station. The synchronization locations s_{syn} are different for different frequencies. They can be computed based on the fact that they correspond to $\omega = 0.1825$. The values of s_{syn} for the 15 frequencies considered in this paper have been computed and tabulated in Table 1.

The wave patterns in the flow field can be represented by contours of real or imaginary parts of the velocity perturbations obtained by a temporal FFT analysis of the instantaneous simulation results. Figure 5 shows the contours of the real part of the velocity perturbations in the computational flow field for the frequency of $f^* = 119.4kHz$ ($n = 8$). Only the early part of the computation domain is shown in the figure in order to show more clearly the detail of the wave structure. The contours show the development of perturbations of a fixed frequency starting from the blowing-and-suction region. The outer boundary of the computational domain is the bow shock. The wave structures induced by the forcing is a typical of those of the second mode instability waves.

Figures 6 to 8 show the distributions of amplitudes of pressure perturbations, $|p_n(x, y)|$, for different forcing frequencies along the cone surface. The pressure perturbation amplitudes, $|p_n(x, y)|$, are obtained by a temporal FFT calculation. Each line in these figures represents one of the 15 frequencies given by Eq.

(11), where the value of n is marked on the lines in the figures. The frequency for a value of n can be found in Table 1. In these figures, the relative amplitudes in the blowing/suction forcing waves for each frequency are different because they are chosen be the same as a previous study.[19]

These three figures show that, for all three cases, the receptivity to surface blowing/suction leads to the clear development of unstable second mode for the three frequencies at $n = 7, 8, 9$, varying from 104.5 kHz to 134.3 kHz. The strong amplitude growth is consistent with the instability of the second mode shown in Figs. 2 and 4.

On the other hand, for the frequency of 149.2 kHz ($n = 10$), the second mode excitation depends on the blowing/suction locations. For Case 1 where the blowing/suction slot is located at an early station of $s = 100$, Fig. 6 shows the amplitude growth of the second mode. However, when the blowing/suction slot moves downstream to $s = 150$ and $s = 210$ for Case 2 and Case 3 respectively, Figs. 7 and 8 show no clear development of instability waves in the boundary layer, even though the second mode is predicted to be unstable by LST (Figs. 2 and 4). The simulations show a very consistent relation of the second mode excitation with the surface blowing/suction location relative to the synchronization location shown in Fig. 3. For the frequency of 149.2 kHz, Table 1 shows that the synchronization location is $s_{syn} = 122$. The results show that the second mode waves are strongly excited when the blowing/suction location is upstream of s_{syn}.

The effect of blowing/suction locations on the receptivity of the second mode can be shown more clearly when the results of different blowing/suction location but with the same frequency are compared. Figures 9 to 12 compare the pressure perturbation amplitudes for the three cases of different blowing/suction locations at four frequencies. For 104.5 kHz ($n = 7$), the blowing and suction locations for all three cases are upstream of its synchronization location of $s_{syn} = 249$. Figure 9 shows that the second mode are strongly excited for all three blowing/suction locations. The results also show an interesting property that the amplitudes of the second modes developed in the boundary layer are almost independent of the blowing/suction locations, as long as they are upstream of s_{syn}. Figure 10 shows similar results for the frequency of 150.6 kHz ($n = 8$), where the blowing/suction locations for the first two cases, but not the third case, are upstream of $s_{syn} = 150.6$ for this frequency. Again, the first two cases induce the second mode of about the same strength. The second mode excitation is not sensitive to the location of blowing/suction as long as it is upstream of s_{syn}. On the other hand, the second mode magnitudes are almost an order of magnitude weaker when the blowing/suction location is downstream of s_{syn}. Similar results of strong correlation between the receptivity and the blowing/suction location relative to s_{syn} can also be observed for the frequency of 149.2 kHz ($n = 10$) and 164.1 kHz ($n = 10$) (Figs. 11 and 12). Figure 11 shows when the blowing/suction location moves downstream of s_{syn}, the second mode excitation decreases rapidly. In the case of 164.1 kHz (Fig. 12), the second mode is developed when the blowing/suction location is upstream of s_{syn} as expected. The second mode is not excited at all when the blowing/suction location is far downstream of the synchronization location.

B. Simulation-Experiment-LST Comparison on Second Mode Instability

The simulation results show the excitation of strong unstable second mode when the blowing/suction location is upstream of s_{syn} for frequencies in the range of 104 kHz to 149 kHz. The second mode excitation is not sensitive to the location of blowing/suction as long as it is upstream of s_{syn}. In this section, the wave numbers, growth rates, wave speeds, and N factors of the second mode computed by the receptivity simulations are compared with LST and experimental results. In principle, the eigenfunctions obtained by the receptivity simulations can also be compared with LST and experimental results. Since the eigenfunction comparison has been done in our previous studies,[18,19] the comparison of second-mode eigenfunction between the LST and simulations are not repeated here. It was shown in Zhong and Ma[19] that there is a very good agreement between the second mode eigenfunctions obtained by simulation and predicted by LST. Such comparison was used to identify the computed wave modes in the simulations.

The growth rates, wave numbers, phase velocities, and N factors can be extracted from the unsteady

simulation results of each frequency by mean of a temporal Fourier transform. First, the unsteady calculations are carried out until the solutions reach a periodic state in time. Temporal Fourier analysis is then carried out on the local perturbations of unsteady flow variables. A Fourier transform for the perturbation field of an arbitrary flow variable q leads to:

$$q'(x,y,t) = \Re\{\sum_{n=0}^{N} |q_n(x,y)|\ e^{i\,[-n\omega_1 t + \phi_n(x,y)]}\} \tag{13}$$

where $n\omega_1$ is the frequency of the n-th wave mode, $q'(x,y,t)$ represents an arbitrary perturbation variable. The Fourier transformed variables, $|q_n(x,y)|$ and $\phi_n(x,y)$, are spatially varying real variables representing the local perturbation amplitudes and phase angles at the wave frequency of $n\omega_1$. For perturbations on the body surface, we can compute local growth rate α_i, wave number α_r, and N factor from the numerical perturbation fields by,

$$\alpha_i = \frac{1}{|q_n|}\frac{d|q_n|}{ds} \tag{14}$$

$$\alpha_r = \frac{d\phi_n}{ds} \tag{15}$$

$$N = \log(|q_n(s)|/|q_n(s_r)| \tag{16}$$

where the derivatives are taken along the natural coordinate s along the body surface, and s_r is the reference surface station to take the amplitude ratios for N factor calculations. The phase velocity a can then be calculated by using Eq. (8).

If the flow perturbations of the simulation results in a local region of the boundary layer are dominated by a single wave mode (second mode), the parameters, α_r, α_i and N, computed by Eqs. (14) to (16) are the wave numbers, growth rates, and N factors of this mode. In this case, α_i, α_r, and N are smooth functions of s. On the other hand, if the simulation results contain simultaneously multiple wave modes in a local region of the boundary layer, the parameters computed by Eqs. (14) and (16) do not represent the wave numbers, growth rates, and N factors of a single wave mode. Instead, these parameters represent a modulation of two or more wave modes. As a result, the distributions of α_i, α_r and N along the surface direction will be oscillatory functions of s. In this case, further decomposition of different wave components is required in order to obtain the growth rates and wave numbers of the individual wave modes. Therefore it is expected that the comparison will be good when the simulation shows a dominantly strong second mode.

Figure 13 compares the second mode growth rates at the surface station of $s = 175$. This is the station where most previous LST calculations were compared with experimental results (Fig. 2). In the figure, the LST results shown were computed by Zhong and Ma in an earlier paper.[19] Two sets of experimental growth rates of Stetson are plotted. The first set (labeled as Stetson's Experiment II in the figure) is the growth rates published in Stetson's original 1984 paper.[4] The second set (Stetson's Experiment I) are those calculated by the current author based on the new published experimental results (Fig. 28 of Schneider's review paper[21]). The growth rates of the current simulation of four frequencies ($n = 8, 9, 10, 11$) are plotted in the figure. These four frequencies show second mode excitation at this location in the simulation results. This figure shows that the growth rates of the full Navier-Stokes simulation agree very well with the LST results. On the other hand, the newly published experimental growth rates are much closer to those of the original LST and experimental results. The new experimental results are about 8% and 14% different from the LST and experimental results. The good agreement in wave numbers is also observed in second mode predicted by LST and by Navier-Stokes simulation in Fig. 14 for the 175 surface station.

Schneider suggests that the region between 195 and 215 nose radius contains experimental results which are better for linear stability comparison because the experimental results are linear and clearly above the background noise. Figure 15 and 16 show both growth rate and wave number comparison for the surface station of $s = 215$. Again, the numerical simulation results in both growth rates and wave numbers agree

very well with those of LST. In addition, the experimental growth rates based on the newly published results agree reasonably well with the LST and experimental results: 3% difference in wave number and 12% difference in growth rate for the peak growth rate. This is a reasonable agreement considering the fact that the wall surface is not perfectly adiabatical in the experiment.

Schneider[17, 21] suggested that the N factor or the amplitude ratio are better parameters for numerical-experimental comparisons because they are surface integration of the growth rates. Schneider used the surface station of $s = 195$ as a reference station to compare the amplitude ratio or the N factor in the linear growth region of $195 \leq s \leq 215$. In this paper, similar comparison is also done between the numerical simulation, LST, and experimental results in the linear growth region. Figure 17 compares the amplitude ratios ($e^N = A/A_{ref}$) at the surface station of $s = 215$, while the reference station is taken to be $s = 195$. The LST results of Lyttle et al.[20] are plotted for comparison. The figure shows a good agreement between the simulation and the experimental results for the amplitude ratios. The agreement is particular good for the frequencies of 119.4 ($n = 8$) and 134.3 kHz ($n = 9$). These two frequencies are among the most unstable second modes at this surface station. The simulation results also agree reasonably well with the LST results of Lyttle et al.

The variations of N factor as a function of s (at a fixed frequency) are also compared between the experimental and simulation results. Figures 18 to 21 compare the N factor as a function of s for four frequencies in the range of unstable second mode (104.5 kHz to 149.2 kHz). The figures show that for the two frequencies of strongest second mode instability (Fig. 19 for 119.4 kHz and Fig. 20 134.3 kHz), the experimental N factors agree very well with the simulation results in the "linear growth region" of $195 \leq s \leq 215$. As expected, the agreement is not good when s is upstream of this region because the background noise is too strong in the experimental results, while the agreement is not good when s is downstream of this region because the nonlinear higher harmonics becomes significant in the experimental results. In addition, the agreement is not good for the higher frequency of 149.2 kHz because the second mode excitation is not very strong at this frequency. The experiment data at this frequency may be affected by nonlinear effects.

Compared to the N factors, the growth rate is a more difficult parameter for numerical-experimental comparison because it is the derivative of the N factors. The experimental and numerical results can be easily affected by background noise or modulation by some other weak wave modes in the boundary layer. Figures 22 and 23 compare the growth rates as a function of s at a fixed frequency for the two frequencies of 119.4 kHz ($n = 8$) and 134.3 kHz ($n = 9$). The simulation results near the blowing/suction slots contain multiple modes due to initial transients. As a results the growth rates computed by the simulation before the second modes are dominant show strong oscillation. After the second mode becomes dominant, the growth rates represent those of the second mode. Again the figures show that the growth rates in the "linear growth region" around $s = 200$ are close to those of the simulation. The experimental growth rates away from this region do not agree with the simulation because of background noise or nonlinear effects in the experimental results.

The growth rates of LST (Zhong and Ma[19]) are also compared with simulation and experimental results in Fig. 22 for the frequency of 119.4 kHz. The figure shows that the LST predicts the same peak second mode location while under-predicting the peak growth rate amplitude by 5.6%. The difference is likely to be caused by the parallel flow assumption used in the LST analysis. Nevertheless, the agreement is reasonably good, considering the different models used in the two approaches. Figure 24 compares the second-mode wave numbers of the same frequency between LST prediction and those computed for the three cases of wall blowing/suction simulations. Once the second modes are excited in the simulation, the wave numbers of the simulation agree very well with those of LST. A similar comparison can also be done by comparing the wave speed between LST and the three cases of simulation. Figure 25 show that such a wave speed comparison for frequency of 119.4 kHz. The wave speeds of both the second mode and a stable mode I are plotted in the figure. The figure shows that the second modes are directly excited by wall blowing/suction. Once the second mode is excited in the simulation, the wave speeds of the simulation agree very well with those of the second mode predicted by LST.

VI. CONCLUSIONS

The growth rates of Mach 7.99 flow over a 7° half-angle blunt cone corresponding to Stetson et al.'s boundary-layer stability experiments have been studied in this paper by comparing results of numerical simulation, experiments, and LST. The receptivity to the wall blowing/suction at three locations is used to excite the second modes in the simulation. The objective of this study is to resolve the long standing disagreements on the second mode growth rates between the experimental measurement and LST predictions. The validation of the accuracy of LST and numerical simulation has practical significance because LST calculations are the foundation of the e^n transition prediction method. In addition, such validation studies are also important because though numerical simulations have become a powerful tool in studying high speed boundary layer transition, they have not been experimentally validated. Experimental validation for such simulations is urgently needed.

The main conclusions of the current study are:

- The growth rates and wave numbers of LST agree very well with those computed by numerical simulation. For the case of 119 kHz, the LST predicts about the same peak second mode location while under-predicting the peak growth rate amplitude by 5.6%. The difference is likely to be caused by the parallel flow assumption used in the LST analysis.

- The experimental amplitude ratio, N factor, and growth rates agree reasonably well with those of the simulation in the "linear growth region" of $195 \leq s \leq 215$ for the frequencies near the peak second-mode instability. As expected, the agreement is not good outside of the linear region due to either the background noise being too strong or because the nonlinear effects become significant in the experimental results. Therefore, the experimental results do agree reasonably well with the simulations and LST results when the experimental results are in the linear region.

- Overall, the simulation and LST results are accurate in predicting second mode growth in the current hypersonic boundary layer. LST used in the e^n method should be an accurate prediction tool for the second instability in such boundary layers.

- The receptivity of the second mode to wall blowing/suction is also studied by simulations for the effects of different blowing/suction locations on receptivity. The results show that second modes are strongly excited when the blowing/suction slot is upstream of the synchronization point. The induced second mode amplitudes are almost the same for different blowing/suction locations, as long as they are upstream of the synchronization point. On the other hand, the second mode excitation becomes substantially weaker when the blowing/suction location is downstream of the synchronization points. As the location moves further downstream, the second mode excitation decreases rapidly. Therefore, the synchronization location between stable mode I and the second mode plays an important role in the receptivity process.

Acknowledgments

This work was sponsored by the Air Force Office of Scientific Research, USAF, under AFOSR Grant #FA9550-04-1-0029, monitored by Dr. John Schmisseur. The views and conclusions contained herein are those of the authors and should not be interpreted as necessarily representing the official policies or endorsements either expressed or implied, of the Air Force Office of Scientific Research or the U.S. Government.

References

[1]Mack, L. M., "Boundary Layer Linear Stability Theory," *AGARD report, No. 709*, 1984, pp. 3–1 to 3–81.

[2]Demetriades, A., "Hypersonic Viscous Flow Over A Slander Cone. Part III: Laminar Instability and Transition," *AIAA paper 74-535*, 1974.

[3]Demetriades, A., "Laminar Boundary Layer Stability Measurements at Mach 7 Including Wall Temperature Effects," *AFOSR-TR-77-1311*, Vol. November, 1977.

[4]Stetson, K. F., Thompson, E. R., Donaldson, J. C., and Siler, L. G., "Laminar Boundary Layer Stability Experiments on a Cone at Mach 8, Part 2: Blunt Cone," *AIAA paper 84-0006*, January 1984.

[5]Maslov, A. A., Mironov, S. G., and Shiplyuk, A. A., "Hypersonic Flow Stability Experiments," *AIAA Paper 2002-0153*, 2002.

[6]Stetson, K. F. and Kimmel, R. L., "On Hypersonic Boundary Layer Stability," *AIAA paper 92-0737*, 1992.

[7]Knight, D. D., "CFD Validation for Hypersonic Flight," *RTO Working Group 10*, Vol. Technologies for Propelled Hypersonic Flight, Subgroup 3, Stage I Report, June 2000.

[8]Kendall, J. M., "Wind Tunnel Experiments Relating to Supersonic and Hypersonic Boundary-Layer Transition," *AIAA Journal*, Vol. Vol. 13, No. 3, pp. 290–299, 1975.

[9]Lachowicz, J. T., Chokani, N., and Wilkinson, S. P., "Boundary-Layer Stability Measurements in Hypersonic Quiet Tunnel," *AIAA Journal*, Vol. 34, No. 12, December 1996.

[10]Goggett, G. P., Chokani, N., and Wilkinson, S. P., "Hypersonic Boundary-Layer Stability Experiments On A Flared-Cone Model at Angle Of Attack In A Quiet Wind Tunnel," *AIAA Paper 97-0557*, January 1997.

[11]Chokani, N., "Perspective: Stability Experiments at Hypersonic Speeds in a Quiet Wind Tunnel," *AIAA Paper 2001-0211*, January 2001.

[12]Malik, M. R., Spall, R. E., and Chang, C.-L., "Effect of Nose Bluntness on Boundary Layer Stability and Transition," *AIAA paper 90-0112*, 1990.

[13]Herbert, T. and Esfahanian, V., "Stability of Hypersonic Flow over a Blunt Body," *AGARD CP-514*, Vol. pp. 28-1 – 12, April, 1993.

[14]Kufner, E., Dallmann, U., and Stilla, J., "Instability of Hypersonic Flow Past Blunt Cones – Effects of Mean Flow Variations," *AIAA paper 93-2983*, June 1993.

[15]Kufner, E. and Dallmann, U., "Entropy- and Boundary Layer Instability of Hypersonic Cone Flows – Effects of Mean Flow Variations," *IUTAM Symposium on Laminar-Turbulent Transition*, Vol. Sendai/Japan, September 1994, pp. 197-204, Springer-Verlag, Berlin, 1994.

[16]Rosenboom, I., Hein, S., and Dallmann, U., "Influence of Nose Bluntness on Boundary-Layer Instabilities in Hypersonic Cone Flows," *AIAA Paper 99-3591*, June 1999.

[17]Schneider, S. P., "Hypersonic Laminar Instability on Round Cones Near Zero Angle of Attack," *AIAA Paper 2001-0206*, 2001.

[18]Zhong, X. and Ma, Y., "Receptivity and Linear Stability of Stetson's Mach 8 Blunt Cone Stability Experiments," *AIAA Paper 2002-2849*, January 2002.

[19]Zhong, X. and Ma, Y., "Numerical Simulation of Leading Edge Receptivity of Stetson's Mach 8 Blunt Cone Stability Experiments," *AIAA Paper 2003-1133*, January 2003.

[20]Lyttle, I. J., Reed, H. L., Shipyluk, A. N., Moslov, A. A., Buntin, D. A., Burov, E. V., and Schneider, S. P., "Numerical-Experimental Comparisons of Second-Mode Behavior for Blunted Cones," *AIAA Paper 2004-97*, January 2004.

[21]Schneider, S. P., "Hypersonic laminar-turbulent transition on circular cones and scramjet forebodies," *Progress in Aerospace Sciences*, Vol. 40, 2004, pp. 1 – 50.

[22]Zhong, X., "High-Order Finite-Difference Schemes for Numerical Simulation of Hypersonic Boundary-Layer Transition," *Journal of Computational Physics*, Vol. 144, August 1998, pp. 662–709.

[23]Ma, Y. and Zhong, X., "Receptivity of a supersonic boundary layer over a flat plate. Part 1: wave structures and interactions," *Jornal of Fluid Mechanics*, Vol. 488, 2003, pp. 31–78.

[24]Ma, Y. and Zhong, X., "Receptivity of a supersonic boundary layer over a flat plate. Part 2: receptivity to freestream sound,," *Jornal of Fluid Mechanics*, Vol. 488, 2003, pp. 79–121.

[25]Ma, Y. and Zhong, X., "Receptivity to Freestream Disturbances of Mach 4.5 Flow over A Flat Plate," *AIAA Paper 2002-0140*, January 2002.

[26]Fedorov, A. V. and Khokhlov, A. P., "Receptivity of Hypersonic Boundary Layer to Wall Disturbances," *Theoretical and Computational Fluid Dynamics*, Vol. 15, 2002, pp. 231–254.

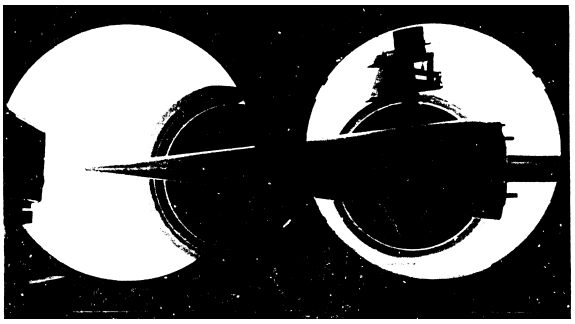

Figure 1. The 7° half-angle blunt cone of Stetson's Mach 7.99 stability experiments (Stetson et al. 1984).

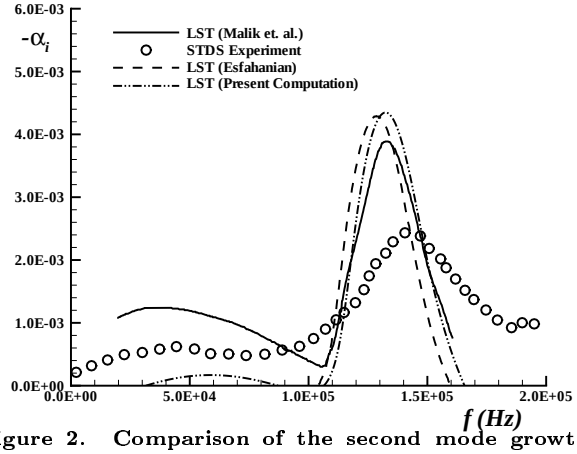

Figure 2. Comparison of the second mode growth rates predicted by LST and experiments by Stetson et al. (1984) at $s = 175$ (Zhong and Ma, 2003).

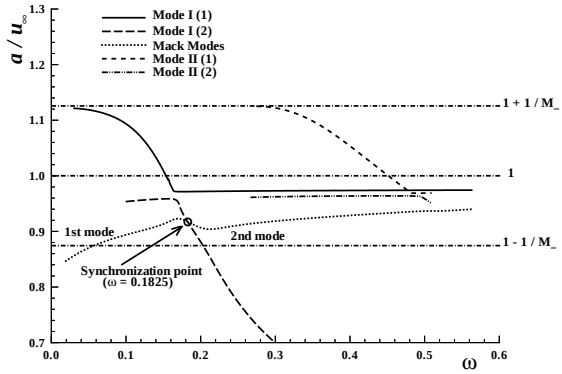

Figure 3. Distributions of the phase velocities of three discrete modes as functions of frequencies at $s = 175$ (Zhong and Ma, 2003).

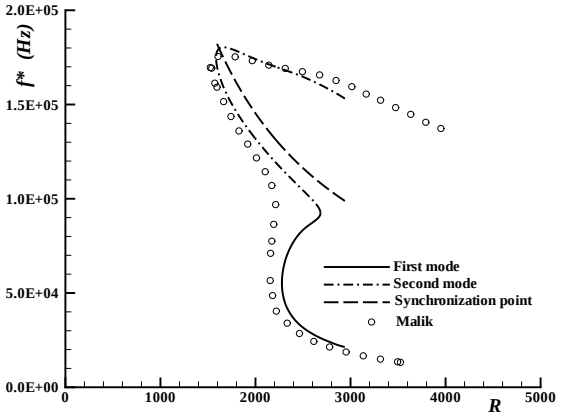

Figure 4. Comparison of the current neutral stability curve of the Mack modes with Malik's (1990) results (Zhong and Ma, 2003).

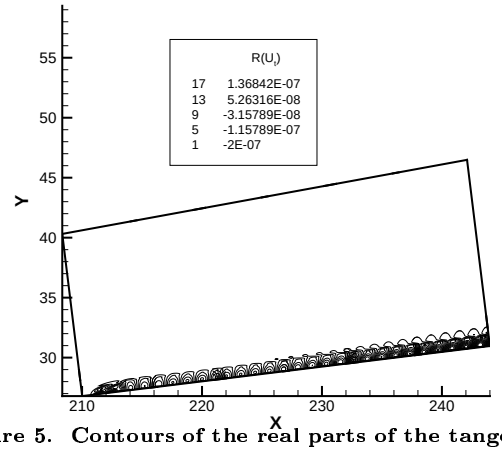

Figure 5. Contours of the real parts of the tangential velocity perturbations at 119.4 kHz ($n = 8$) for Case 3.

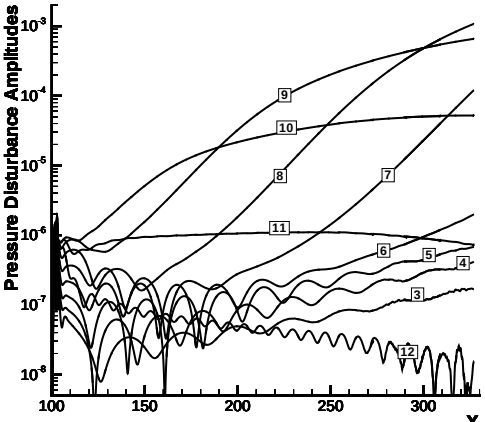

Figure 6. Amplitude distribution of pressure perturbations along cone surface for Case 1.

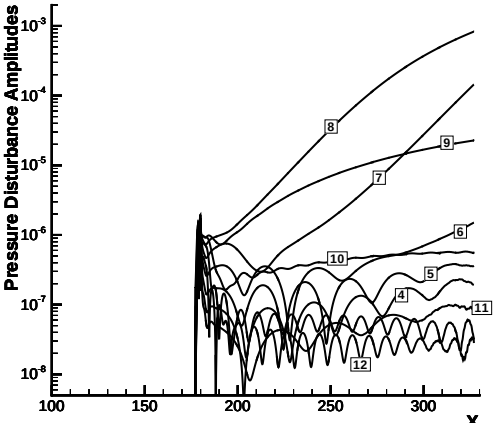

Figure 7. Amplitude distribution of pressure perturbations along cone surface for Case 2.

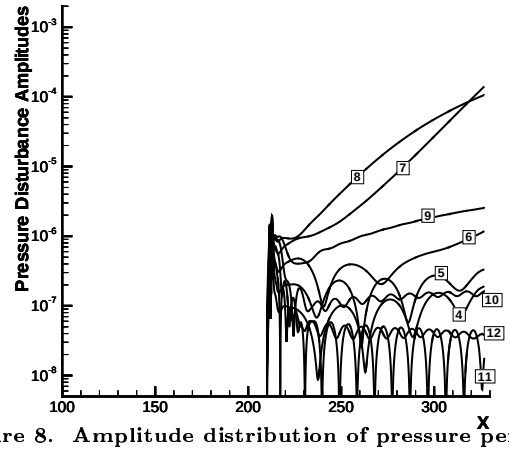

Figure 8. Amplitude distribution of pressure perturbations along cone surface for Case 3.

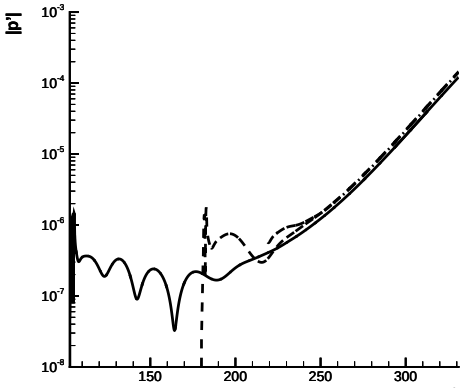

Figure 9. Comparison of pressure perturbation amplitudes for three different location of blow-and-suction for a fixed frequency of 104.5 kHz ($n = 7$).

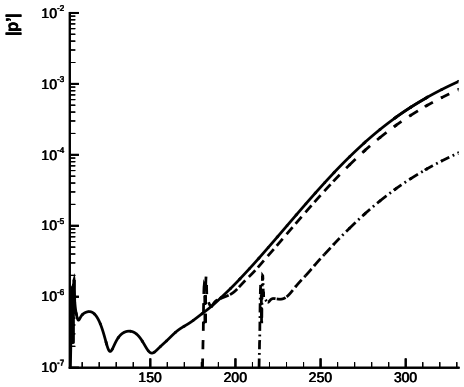

Figure 10. Comparison of pressure perturbation amplitudes for three different location of blow-and-suction for a fixed frequency of 119.4 kHz ($n = 8$).

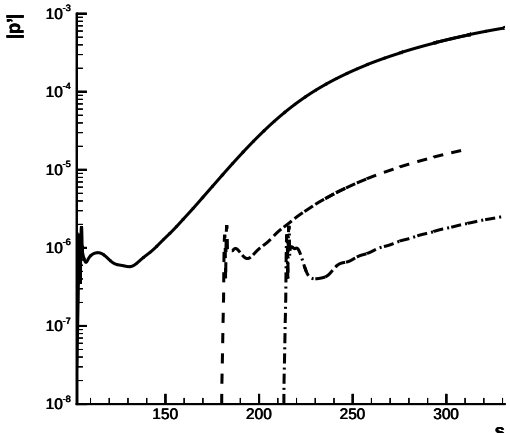

Figure 11. Comparison of pressure perturbation amplitudes for three different location of blow-and-suction for a fixed frequency of 134.3 kHz ($n = 9$).

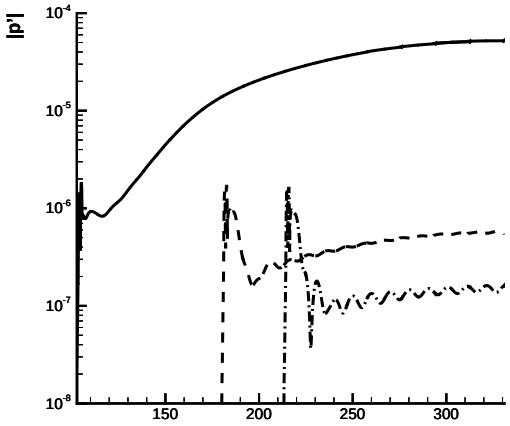

Figure 12. Comparison of pressure perturbation amplitudes for three different location of blow-and-suction for a fixed frequency of 149.2 kHz ($n = 10$).

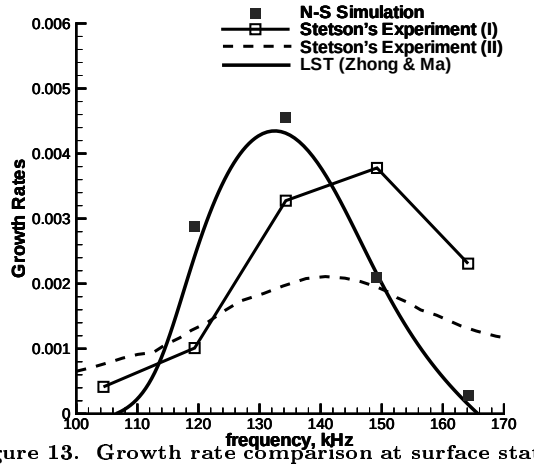

Figure 13. Growth rate comparison at surface station of $s = 175$.

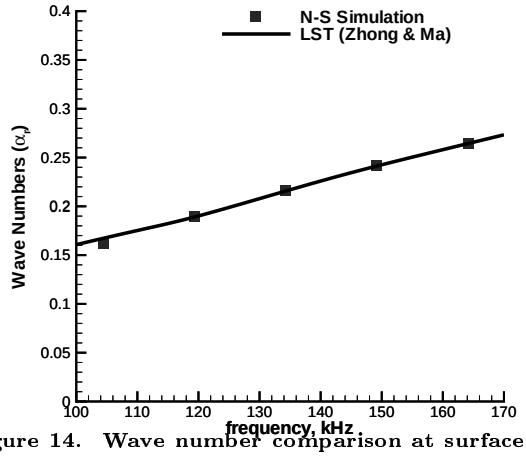

Figure 14. Wave number comparison at surface station of $s = 175$.

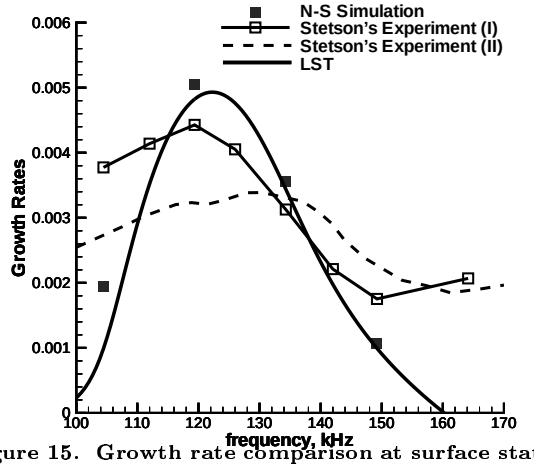

Figure 15. Growth rate comparison at surface station of $s = 215$.

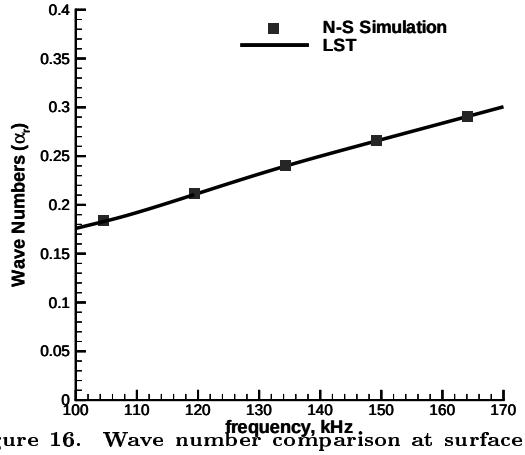

Figure 16. Wave number comparison at surface station of $s = 215$.

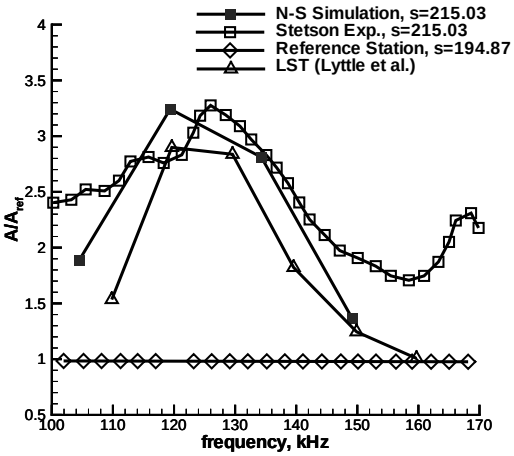

Figure 17. Amplitude ratio ($e^N = A/A_{ref}$) comparison at surface station of $s = 215$. The reference station is taken to be $s = 195$.

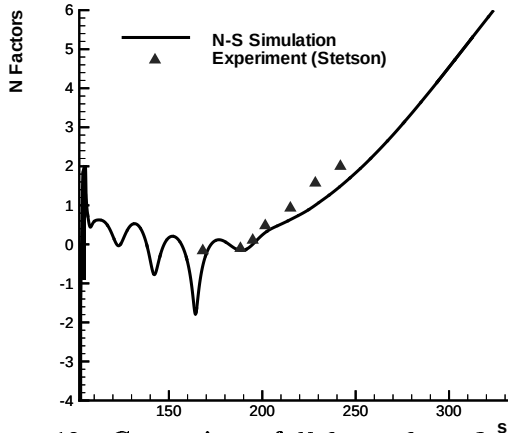

Figure 18. Comparison of N factor for a fixed frequency of 104.5 kHz ($n = 7$).

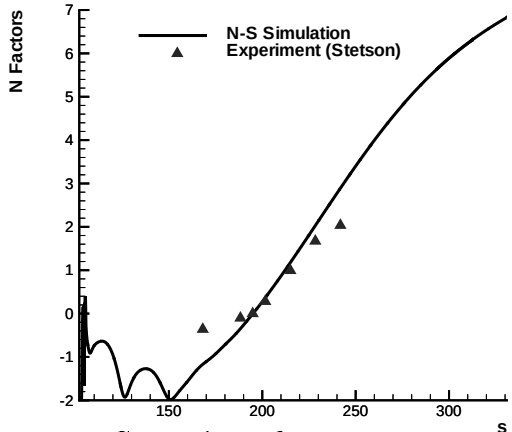

Figure 19. Comparison of N factor for a fixed frequency of 119.4 kHz ($n = 8$).

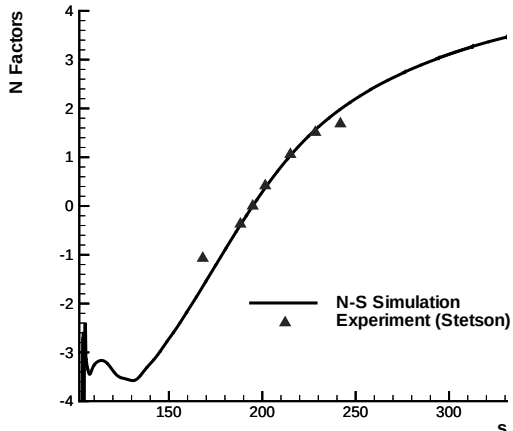

Figure 20. Comparison of N factor for a fixed frequency of 134.3 kHz ($n = 9$).

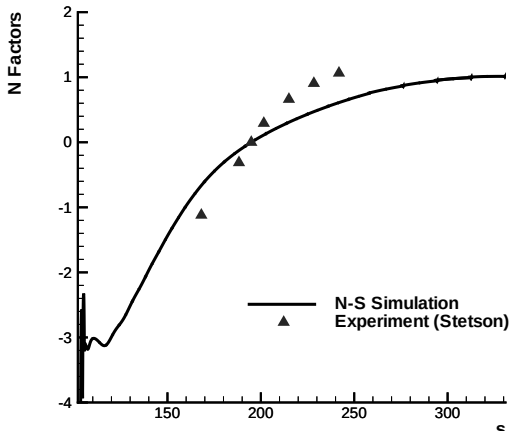

Figure 21. Comparison of N factor for a fixed frequency of 149.2 kHz ($n = 10$).

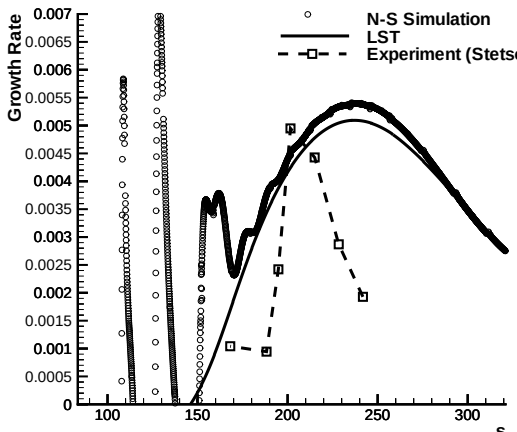

Figure 22. Comparison of growth rates for a fixed frequency of 119.4 kHz ($n = 8$).

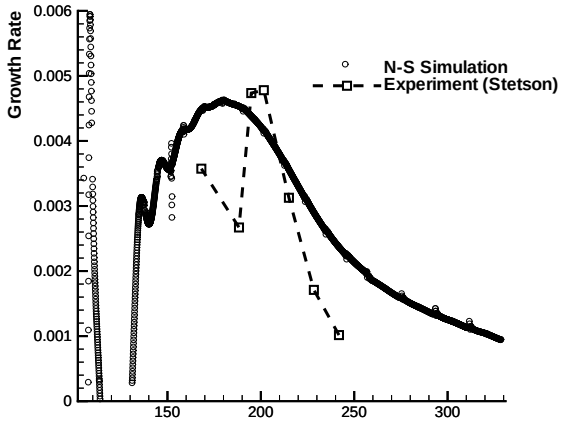

Figure 23. Comparison of growth rates for a fixed frequency of 134.3 kHz ($n = 9$).

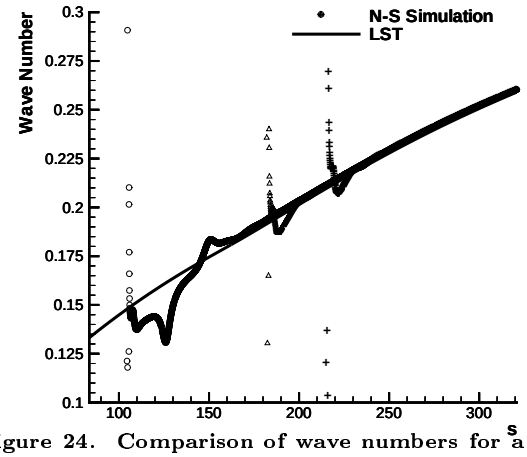

Figure 24. Comparison of wave numbers for a fixed frequency of 119.4 kHz ($n = 8$).

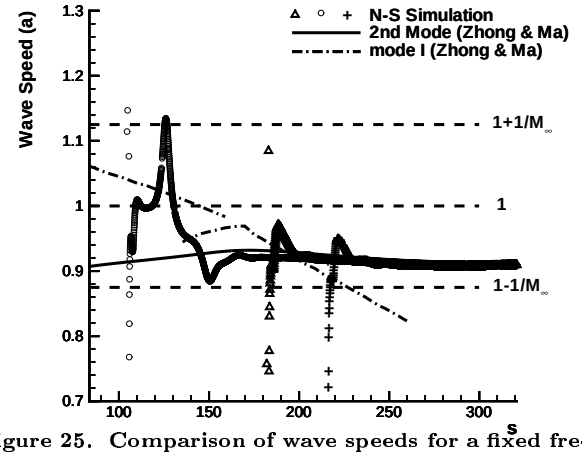

Figure 25. Comparison of wave speeds for a fixed frequency of 119.4 kHz ($n = 8$).